Faraday Discussions

Accepted Manuscript

This is an Accepted Manuscript, which has been through the
Royal Society of Chemistry peer review process and has been accepted
for publication.

Accepted Manuscripts are published online shortly after acceptance,
before technical editing, formatting and proof reading. Using this free
service, authors can make their results available to the community, in
citable form, before we publish the edited article. We will replace this
Accepted Manuscript with the edited and formatted Advance Article as
soon as it is available.

You can find more information about Accepted Manuscripts in the
Information for Authors.

Please note that technical editing may introduce minor changes to the
text and/or graphics, which may alter content. The journal's standard
Terms & Conditions and the Ethical guidelines still apply. In no event
shall the Royal Society of Chemistry be held responsible for any errors
or omissions in this Accepted Manuscript or any consequences arising
from the use of any information it contains.

Exploring cooperative porosity in organic cage crystals using *in situ* diffraction and molecular simulations

Linjiang Chen,[a,b] Yu Che,[a,b] Andrew I. Cooper,[a,b] and Samantha Y. Chong*[a]

* Corresponding author

[a] Materials Innovation Factory and Department of Chemistry, University of Liverpool, 51 Oxford Street, Liverpool, L7 3NY, UK. E-mail: s.chong@liverpool.ac.uk

[b] Leverhulme Research Centre for Functional Materials Design, Materials Innovation Factory and Department of Chemistry, University of Liverpool, 51 Oxford Street, Liverpool, L7 3NY, UK.

ORCID iD: Linjiang Chen, 0000-0002-0382-5863; Andrew I. Cooper, 0000-0003-0201-1021; Samantha Y. Chong, 0000-0002-3095-875X.

Abstract

A porous organic cage crystal, **α-CC2**, shows unexpected adsorption of sulphur hexafluoride (SF_6) in its cage cavities: Analysis of the static crystal structure indicates that they are occluded, as even the smallest diatomic gas, H_2, is larger than the window of the cage pore. Herein, we use *in situ* powder X-ray diffraction (PXRD) experiments to provide unequivocal evidence for the presence of SF_6 inside the 'occluded' cage voids, pointing to a mechanism of dynamic flexibility of the system. By combining PXRD results with molecular dynamics simulations, we build a molecular level picture of the cooperative porosity in **α-CC2** that facilitates the passage of SF_6 into the cage voids.

Introduction

The field of crystalline porous materials spans a range of chemically diverse solids, from classical inorganic zeolites to more contemporary metal-organic frameworks (MOFs) and organic porous crystals. In recent years, MOFs have begun to fulfil their promise as 'designed' functional materials, finding applications in areas such as ionic conductivity,[1] catalysis,[2] and drug delivery.[3] Kitagawa has highlighted the importance of dynamic structural behaviour in these frameworks for the next generation of porous network materials,[4] and the ability of solids to react to external stimuli offers the promise of adaptable, responsive and multifunctional materials. The implications of understanding the structural response of soft crystals to external stimuli extend beyond functions related to porosity. Recent research into crystals exhibiting properties such as plasticity[5] and thermo/photo-salient behaviour[6,7] shows how microscopic structural flexibility can extend into the macroscopic realm. This in turn suggests the possibility of designing functional, all-organic devices, such as actuators and sensors, for use in energy and data storage applications.

Soft porosity in molecular crystals

Porous molecular crystals are still relatively uncommon,[8] despite a recent focus on the development of new types of porous molecules such as supramolecular (and hydrogen-bonded) organic frameworks[9–13] and organic cages.[14–17] The likelihood of molecular crystals forming ordered solids that can undergo responsive structural rearrangements would intuitively seem higher than for framework solids[18] because the interactions between the constituents of the crystal—the intermolecular forces—are weaker and should be more readily overcome[5] in comparison with the stronger coordinative or covalent bonding in frameworks such as MOFs or covalent organic frameworks (COFs). Polymorphic phase transitions induced by gentle stimuli such as mild heating[19,20] or grinding[21,22] are common, even in densely-packed molecular solids. The lack of strong extended bonding in porous crystals composed of discrete molecules allows for changes in molecular conformation accompanied by limited disruption to the crystal packing.[23] Furthermore, the crystals can accommodate transient local rearrangements that do not extend across the crystal; hence individual molecules can readily exhibit dynamic flexibility within their covalent skeleton, and also in terms of their position and orientation in the crystal structure, without necessarily resulting in longer range perturbation of the crystal.[24–27] As a result, the definition of "porosity" is a rich concept for molecular crystals, which can be divided into three classes: static porosity, dynamic porosity, and cooperative porosity, depending on how pore interconnectivity is related to the structural flexibility of the host.[24] Static porosity refers to existence of a connected pore topology in a static structure, as probed by a specific guest molecule. Dynamic porosity arises when the inherent molecular and lattice flexibility of the host extends the connected pore network to otherwise occluded voids; for example, cage cavities. Finally, cooperative porosity only exists when the influence of a guest molecule is required to facilitate guest transport within a flexible host.

Guest response in organic cage crystals

Porous organic cages are covalently-bonded discrete molecular species that contain an enclosed intrinsic pore that is accessible via openings in the molecular backbone.[14,28–30] A guest must pass through these cage 'windows', and hence their size and shape modulates the guests that can enter the individual cage host pore. For cages to exhibit porosity in the solid state, guests must either be able to access the internal cage pore (intrinsic porosity) or the cage molecules must pack in such a way that accessible voids are created between the molecular host (extrinsic porosity), or some combination of the two. In the case of intrinsic porosity, the cage molecule itself must maintain its shape so that the internal pore persists in the absence of guests, and a pathway must exist to access the cage pore. To exhibit purely extrinsic porosity, accessible voids are created by the inefficient packing of the molecules and collapse or preservation of the cage pore is irrelevant.

Porous organic cage crystals have been reported previously to exhibit guest-triggered polymorph switching,[31] in which the rearrangement of the cage packing orders across the entire crystal, and also more limited and dynamic structural behaviours[24,25,32,33] that allow guests to access pore volume in the crystal expected to be inaccessible to guests of that size. Several studies of the unexpected diffusion of large guests in porous cage crystal have been reported previously. The prototypical [4+6] imine-linked porous organic cage crystal **α-CC3** has been shown to allow diffusion of guest molecules, such as *para*-xylene and xenon, whose diameters are larger than the narrowest point in its pore network when considering a static view of the **α-CC3** crystal structure.[32,33] Based on 'static' porosity analysis, the intrinsic cage voids of another porous organic cage crystal **α-CC2** (Figure 1) are disconnected from adjacent one-dimensional extrinsic pore channels (Figure S1), even for the smallest diatomic gas, H_2.[24] Despite this, it has been shown experimentally to adsorb large gases such as CO_2 and xenon in its cage voids.
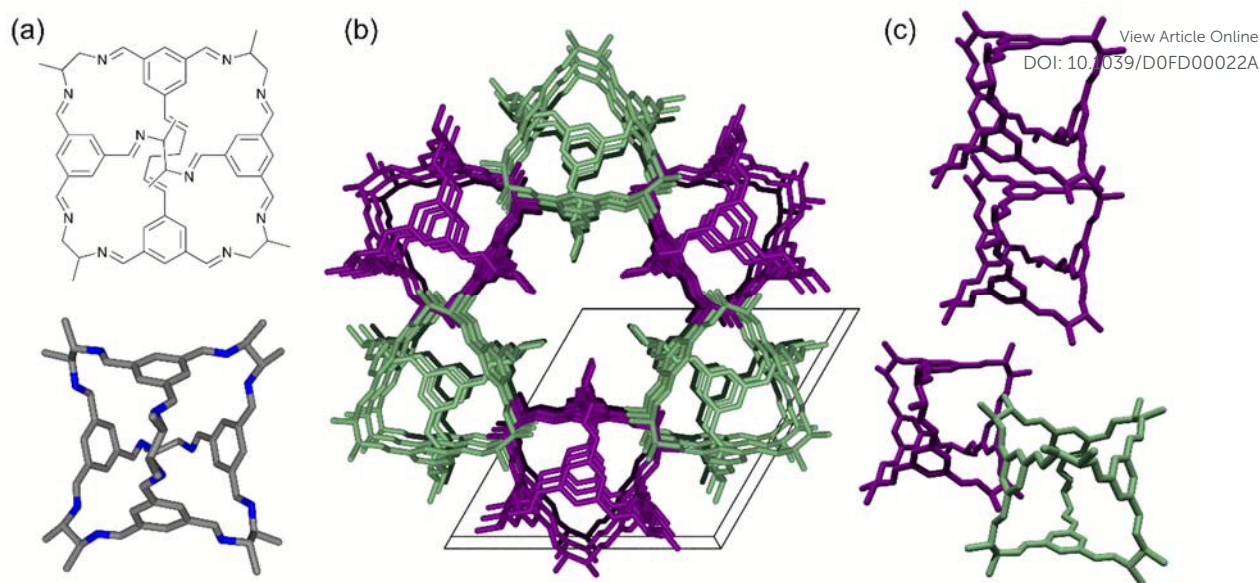
Figure 1. (a) The chemical connectivity of the **CC2** cage molecule (*top*) and its three-dimensional conformation (*bottom*; carbon shown in grey; nitrogen atoms in blue; hydrogen atoms omitted for clarity). (b) Crystal structure of **α-CC2** viewed parallel to the crystallographic *z*-axis, showing the extrinsic 1-D pore network running between hexagonal layers of cages at the centre. (c) The structure is composed of offset stacks of cages arranged window-to-arene (*top*) in alternating orientations, shown by purple and green colouring (Figure S1). Within the layer, cages in neighbouring stacks are arranged vertex-to-window (*bottom*), resulting in three windows of a cage being occluded by the vertices of adjacent cages.

A series of porous organic cages was studied for the adsorption of sulphur hexafluoride (SF_6), and the SF_6 uptakes of the materials were found to be considerably higher than would be expected from their static pore structures.[25] Molecular simulations indicated that in **α-CC3** the presence of a SF_6 molecule in the cage window causes the 'pore envelope'—that is, the distribution of cage window diameters sampled across a molecular dynamics trajectory—to shift dramatically in comparison to the empty **α-CC3** crystal structure and when SF_6 occupies a location inside the cage pore. This indicates the cooperative component of the structural response, which results in the increased flexibility of the cage molecule, and hence the observed 'soft' porosity of the structure. This helps to rationalise the case where diffusion through the pore network is limited by the size of the pore window. In the case of **β-CC13**, the uptake of SF_6 can only be rationalised by the guest having access to the extrinsic voids in the structure, which are expected to be disconnected from the main pore network that passes through the cage pores and windows. The apertures that allow access to the extrinsic sites, formed at the meeting of six vertex functionalities, have a diameter of approximately 3.1 Å;[25] that is, far smaller than the kinetic diameter (5.5 Å) of SF_6. *In situ* XRD suggests that loading SF_6 into the structure induces a reduction in the shorter range order of the solid, consistent with local disordering of the cage molecules. This could enable the large guest to access and occupy extrinsic space, while preserving the long-range average periodicity of the molecular packing.

While it has been possible to explore how diffusion pathways dynamically develop for such bulky guests when a probable route can be deduced from the pore topology,[32–34] there have been fewer studies in systems where it is difficult to intuitively assume a pathway that would seem to require significant local structural rearrangement of the host. Here, we explore the dynamic and cooperative nature of interactions between the crystalline structure of a purely organic porous cage molecule, **CC2**, and the bulky guest sulphur hexafluoride, SF_6. The organic cage crystal, **α-CC2**, was shown previously to exhibit significant SF_6 uptake.[25] The SF_6 molecule is far larger than would be expected to be able to diffuse into the intrinsic pores of the host crystal; here, we use *in situ* crystallographic methods to show that the 'soft' crystal structure allows the large guest to occupy both the connected pore network and also to enter the internal cage pores, despite its entry via the cage windows being heavily occluded. This provides unequivocal evidence of an unexpected dynamic flexibility of the crystalline structure. We couple the experimentally determined guest-loaded crystal structure with constrained molecular simulations to elucidate the pathway of the guest and to understand the flexibility of the cage molecules and their crystal packing in the presence of the guest species.

Experimental and computational methods
Materials
1,3,5-Triformylbenzene was purchased from Manchester Organics; other reagents and solvents were purchased from Sigma Aldrich. All chemicals were used as received.

CC2 was synthesised as previously described[14] and crystallised as the solvated α-form directly from synthesis. The sample was dried under vacuum at 80 °C for 12 hours.

In situ powder X-ray diffraction
Powder X-ray diffraction data (PXRD) were collected *in situ* under variable pressures of SF_6 gas using the low pressure capillary gas cell[35] on beamline I11 at Diamond Light Source (λ = 0.825737 Å). Samples of **α-CC2** dried in a vacuum oven overnight were finely ground using a pestle and mortar and packed into 0.7 mm diameter borosilicate glass capillaries. The capillary was mounted in the gas cell and secured using epoxy adhesive. The temperature of the capillary was controlled using an Oxford Cryostream Plus.

Initial activation of the sample was carried out by heating the sample to 373 K under dynamic vacuum applied using a turbomolecular pump (approximately 10^{-5} mbar) for 60 min. A baseline diffraction pattern of the evacuated crystal was collected at 273 K using the Mythen II position sensitive detector (PSD).

Due to experimental constraints to minimise release of sulphur hexafluoride–a potent greenhouse gas–the sample was exposed to the maximum pressure of SF_6 gas and the

pressure was then reduced in three steps by applying vacuum. Powder data was collected using the PSD at each pressure. The sample was initially dosed with SF$_6$ at 2.7 bar and allowed to equilibrate at each pressure step for at least 30 minutes or until no further changes in diffraction were observed. Pressures above 1 bar were used in order to achieve equilibrium of the maximum loaded structure within the time constraints of the synchrotron experiment.

Structure determination Powder diffraction data were analysed using *TOPAS-Academic*[36] for pattern indexing, structure solution and refinements. In contrast to the known single crystal structure (*P*-3), the bulk evacuated powder sample was found to be lower symmetry and the pattern was indexed with a triclinic (*P*-1) unit cell consistent with one **CC2** molecule in the asymmetric unit. The triclinic symmetry persisted in the guest-loaded structures. Refined unit cell parameters were extracted using Le Bail refinements.

Structure solution calculations based on the PXRD profile collected for the sample under 2.7 bar of SF$_6$ were carried out using the simulated annealing algorithm implemented in *TOPAS-Academic*.[36] The structural model of the cage consisted of a full **CC2** molecule derived from the published single crystal structure. The methyl functionalities at the vertex were assumed to be fully disordered over the two *exo*-positions with 50 % occupancy at each, as there is insufficient resolution to resolve partial ordering from PXRD. Three SF$_6$ molecules with variable occupancy were included in the model. All fragments were allowed to translate throughout the unit cell and rotate freely. The simulated annealing optimisations were allowed run for 5×10^5 iterations and repeated 10 times independently in order to verify that the solution was located reproducibly. The eight fittest solutions showed minimal differences and the best was selected as the starting point for Rietveld refinement.

Structural refinement of SF$_6$-loaded **CC2** was carried out using geometric restraints on all bond lengths and angles within the cage structure, and planarity restraints on ring moieties. The occupancies of the SF$_6$ molecules were allowed to refine freely. Isotropic displacement parameters were refined for each SF$_6$ site, constrained by atom type. A single isotropic displacement parameter was refined for the light atoms of the cage molecule. Hydrogen atoms were modelled at standard geometries and refined using a riding model, and isotropic displacement parameters were constrained to 1.2 times the parent atom.

Molecular dynamics simulations
All molecular dynamics (MD) simulations were performed using DL_POLY_4.08,[37] with input files (FIELD, CONFIG) generated by DL_FIELD.[38] The OPLS_2005 force-field parameters[39] were used to describe all intra- and inter-molecular interactions for cage molecules. The SF$_6$ molecule was modelled as flexible, by the force field of Olivet and Vega,[40] explicitly considering the S–F bond stretching and the F–S–F angular bending. The isothermal–isobaric (NPT) ensemble at a temperature of 298 K and a

pressure of 1 bar was used for all MD simulations. The Martyna–Tuckerman–Klein variant of thermostat and barostat was used to maintain constant the temperature and pressure. The equations of motion were integrated, with a time step of 0.5 fs, using the velocity Verlet scheme, together with the RATTLE algorithm for solving constraints in potential of mean force simulations. A cutoff radius of 10 Å was applied to all LJ interactions, with energies and forces gradually shifted to zero when approaching the cutoff distance. The smoothed particle mesh Ewald method was used to handle electrostatic interactions. All NPT-MD simulations were first equilibrated for at least 4 ns before statistics were collected for another 2 ns.

The simulation box consisted of a $3\times3\times5$ supercell of the **α-CC2** unit cell, amounting to a total of 90 cage molecules in the system, with periodic boundary conditions exerted in three dimensions. Each **CC2** molecule was randomly assigned one of its four positional isomers because of the disorder of the methyl groups over the vertex *exo* sites of the cage. The initial, static configuration of this "disordered" **α-CC2** supercell, based on the crystallographic coordinates reported by single-crystal diffraction,[14] does not allow the diffusion of even the smallest diatomic gas, H_2, between the intrinsic cage voids and the extrinsic pore channels. A detailed discussion on constructing atomistic models for **α-CC2** can be found in Holden *et al.*[24] Analyses of the pore size, window size and maximum molecular dimension of individual cage molecules were performed with the pywindow package,[41] after pre-processed by in-house python codes.

Results and discussion

Crystal structure of SF$_6$-loaded α-CC2

The PXRD of the activated **α-CC2** sample collected at 273 K was used to determine the lattice parameters of the evacuated crystal structure. As found previously,[24] high resolution synchrotron PXRD data indicates that bulk microcrystalline **α-CC2** adopts a lower symmetry than the trigonal *P*-3 structure determined by single crystal diffraction. The powder diffraction profile was indexed with a triclinic unit cell, consistent with one full **CC2** molecule in the asymmetric unit, indicating the loss of 3-fold symmetry in comparison to the known structure.

On exposure to a high pressure of SF_6, large changes in the relative intensities of the observed diffraction peaks indicated that the guest was incorporated into the crystal lattice (Figure 2a). Sharp diffraction was observed at all pressures, with little broadening observed on uptake, in contrast with previous *in situ* studies of **β-CC13**, where peak broadening suggested uptake-induced local disorder.[25] Additionally, shifts of the diffraction peaks were limited. These observations indicate little disruption of the crystal packing on the diffraction timescale, either locally or requiring significant change in the ordered crystal. The refined unit cell parameters (Table S1) show that the unit cell volume expands by only 1 % at the maximum pressure (2.7 bar) of SF_6, mostly due to expansion of the *a* and *b* cell edges parallel to the hexagonal layers (Figure 2b).
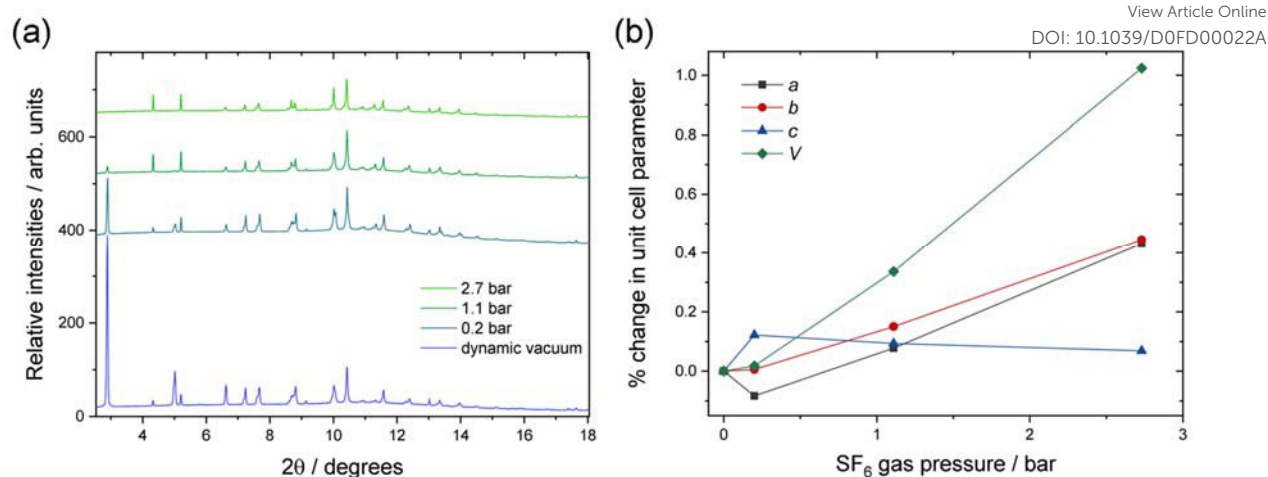
Figure 2. (a) *In situ* synchrotron powder X-ray diffraction data for α-**CC2** collected under SF_6 atmosphere. (b) Lattice parameters extracted by Le Bail fitting (Figure S2) show limited change in the unit cell upon SF_6 uptake.

The structure of SF_6-loaded α-**CC2** was determined from the diffraction profile collected under 2.7 bar of SF_6 gas. Visualisation of the Fourier difference map calculated using the empty α-**CC2** structure indicated the presence of additional electron density in the both the channel and internal cage pore. *Ab initio* structure solution returned models in which three sites are partially occupied by the SF_6 guest: two sites in the extrinsic 1-D channel running parallel to the crystallographic [001] direction and one site within the cage pore.

Rietveld refinement (Figure 3a) indicated that the total guest occupancy is approximately 1.93(1) SF_6 per cage, distributed across the three sites, in the ratio 52(±2):85(±2):56(±3) for the cage pore, first and second channel sites, respectively (Figure 3b-d). This uptake is higher than that previously determined for α-**CC2** by gas adsorption measurements (1.4 per cage),[25] which is likely to reflect the higher pressure used, but may also include sample effects such as a more finely ground or highly crystalline sample[42] used for the diffraction study. The isotropic displacement parameters of the SF_6 molecules are relatively large, reflecting a level of disorder of the gaseous guest that introduces uncertainty in its precise orientation.
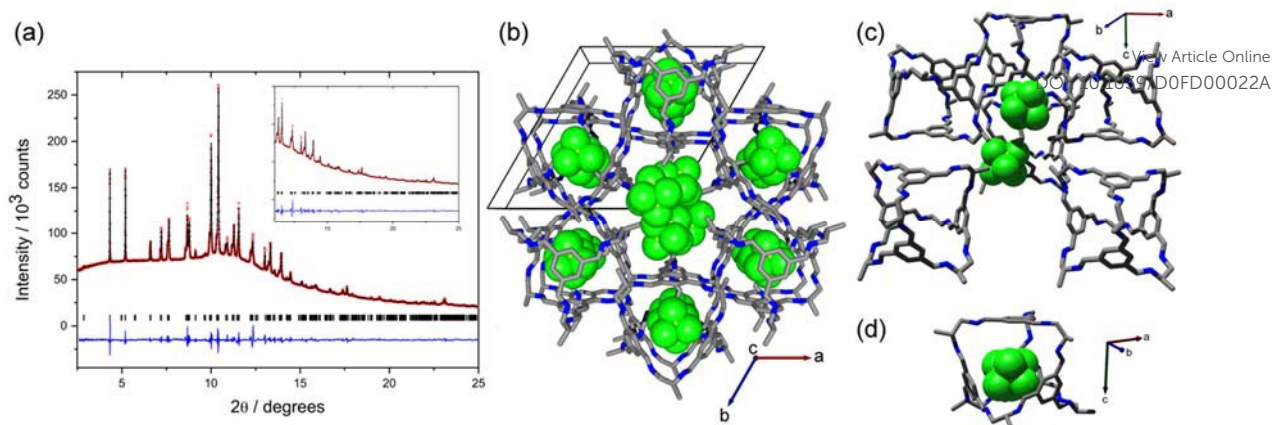
Figure 3. (a) Final observed (red points), calculated (black line) and difference (blue line) profiles for Rietveld refinement of **CC2**•(SF$_6$)$_{1.93}$. Reflections positions are marked below and inset shows high angle fitting at larger scale (R_{wp} = 1.62 %, R_p = 1.10 %, χ^2 = 3.65). (b) Refined structure of **CC2**•(SF$_6$)$_{1.93}$ projected onto the (001) plane. The SF$_6$ guest partially occupies (c) two sites in the 1-D channel and (d) within the intrinsic cage pore.

Comparison of the loaded structure with the host framework shows that the packing of **CC2** molecules is largely undisrupted by the presence of the guest in the crystal (Figure S3). The more highly occupied channel site (Figure 2c, upper site) is surrounded by the arene faces of three **CC2** molecules forming one side of the pore channel, and the methyl groups protruding into the channel enclose the site above and below (Figure S4a). Hence, an SF$_6$ guest occupying this site is likely to be stabilised by F…π interactions[43,44] and weak F…H—C hydrogen bonds. The lower occupancy channel site is closer the narrowed 'necks' of the 1-dimensional channel formed by the methyl groups. It also sits towards one side of the channel interacting with methyl groups of three surrounding cages (Figure S4b). Inside the cage pore, the sulfur hexafluoride guest is displaced from the centre of the cage towards the window (Figure 3d), parallel to the [001] direction, due to the methyl functionalities of adjacent cages penetrating the window (Figure S4c). Interaction between fluorine atoms and the three surrounding arene rings (d = 2.6 – 3.1(1) Å) inside the cage pore may stabilise the guest.

The guest-loaded crystal structure shows that SF$_6$ can occupy both the extrinsic connected pore network and the occluded cage pores, and allows us to rationalise these binding sites. However, the crystallographic timescale cannot provide detailed information on how the large sulfur hexafluoride molecules gain access to the occluded intrinsic sites.

Computational studies

We used simulations to help build a molecular level picture of the mechanism for the diffusion of SF$_6$ from the extrinsic pore channels to the intrinsic cage voids in **α-CC2**. We first ran NPT-MD simulations of **α-CC2** loaded with SF$_6$ for two scenarios: (1) each **CC2** cage molecule was

loaded with one SF_6 molecule inside the cage void; (2) SF_6 molecules were only located in the pore channels. Both MD simulations were run for over 30 ns, and we did not observe a single diffusion event between the intrinsic cage voids and the extrinsic pore channels. This is in line with our previous study of gas adsorption in **α-CC2**,[24] in which transient pore network formation, connecting cage voids and pore channels, was only simulated by MD for H_2 and not for CO_2 or Xe, both smaller in size than SF_6.

Focusing on SF_6 traversing the two kinds of porosity, we resorted to determining the free-energy profiles of possible diffusion pathways between a cage void and its adjacent pore channel. In **α-CC2**, the cage voids are occluded from the pore channels as a result of all four windows of each cage being blocked by a neighbouring cage: for three out of the four windows, it is the adjacent cage vertex (Figure 1c, bottom), while the fourth window is blocked by an arene of the adjacent cage with which the cage stacks along the channel direction (Figure 1c, top). Correspondingly, we defined two diffusion pathways, each connecting a cage void to its nearest pore channel via crossing one cage window blocked by the adjacent cage vertex (*path 1*) or arene (*path 2*). To quantify the changes in free energy along each diffusion pathway, we used constrained MD simulations to calculate the potential of mean force (PMF), a function of the chosen reaction coordinate which specifies the free energy of the system corresponding to a thermal average over all degrees of freedom other than the reaction coordinate. With all the other degrees of freedom averaged out, the motion along the reaction coordinate identifies a highly probable path of diffusive motion which connects the initial state to the final state of the system. The reaction coordinate of each diffusion pathway was defined as the distance between the two molecular entities: for *path 1*, it is the distance between the centre of mass (COM; coloured in red, Figure 4a) of the four cage arenes and the COM of SF_6; for *path 2*, it is the COM (coloured in blue, Figure 4a) of the three nitrogen atoms forming a plane parallel to the window through which the diffusion path crosses. A series of MD simulations was carried out with the system constrained to different points along the reaction coordinate (which was held fixed during the simulation). The diffusion pathway was mapped out by performing constrained MD simulations sequentially—that is, the initial configuration of a simulation was taken as the final configuration of the proceeding one—with increments (in most cases) of 0.2 or 0.4 Å in the reaction coordinate. Integrating the mean constraint forces thereby obtained as a function of the reaction coordinate yielded the changes in free energy along the reaction path (Figure 4).
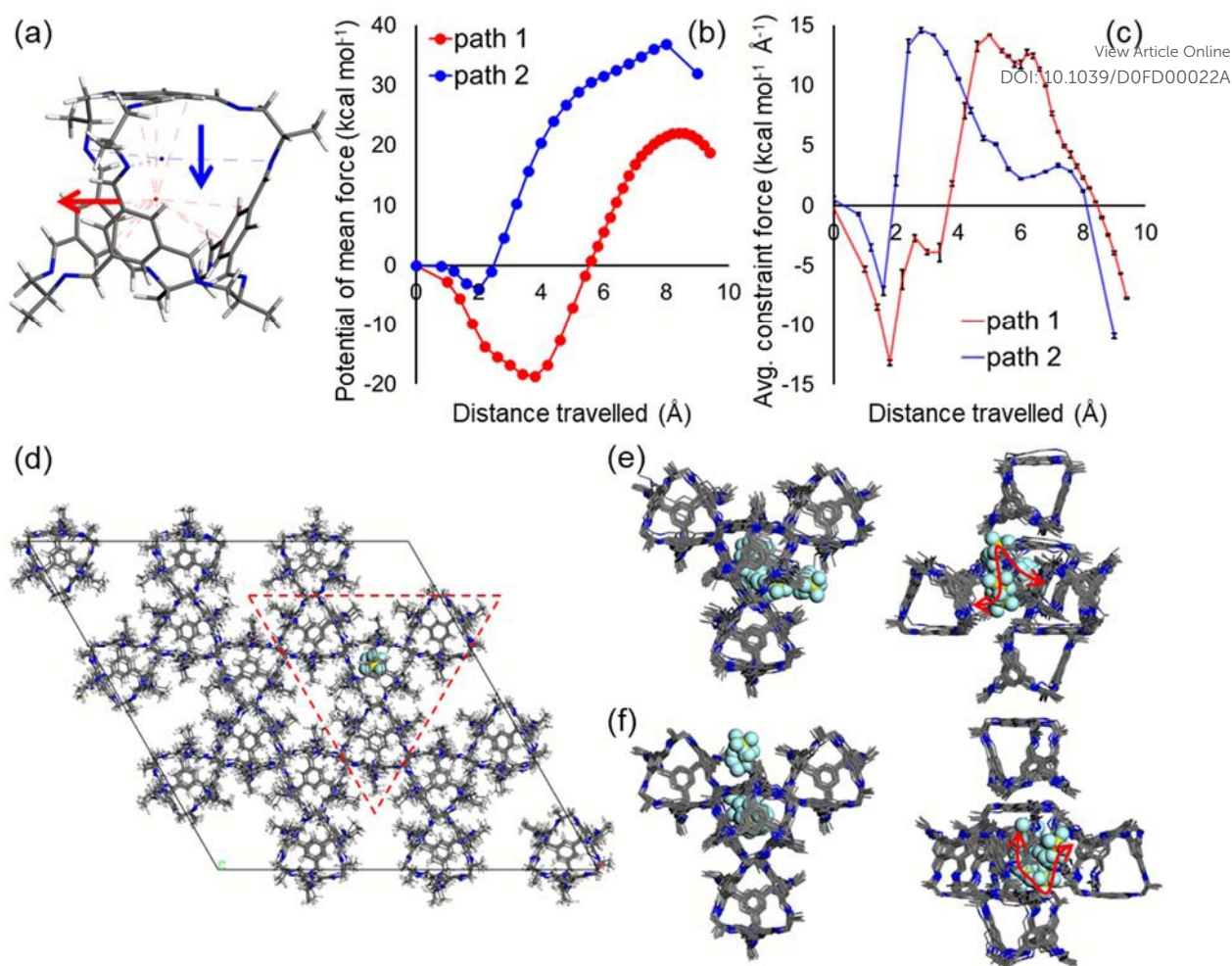
Figure 4. (a) Centre of mass (COM) definitions for the **CC2** cage molecule, together with the COM of SF_6, used to define the reaction coordinate for *path 1* (red) and *path 2* (blue); the red and blue arrows indicate the windows through which *path 1* and *path 2* traverse, respectively. (b, c) The average (avg.) constraint force (c), sampled over the final 500 ps of the MD trajectory at an interval of 1ps, and the corresponding potential of mean force (b), both plotted as a function of the reaction coordinate, which is the distance SF_6 travelled from the pore channel into the cage void; error bars in (c) indicate, for each average constraint force, the maximum value and the minimum value among the five block averages, each covering 100 ps, over the 500 ps trajectory. (d) One snapshot of the simulation box for a PMF calculation, comprising a 3×3×5 supercell of **α-CC2** with one SF_6 molecule in it. (e, f) Overlay of system configurations along the diffusion pathways for *path 1* (e) and *path 2* (f), showing only the central cage— which the SF_6 molecule diffuses into and out of—and the adjacent cages in the region marked out by the red triangle in (d), with all other cages omitted for clarity.

Potential of mean force calculations reveal that the underlying mechanisms for SF_6 diffusion along *path 1* and *path 2* are different. Simulated atomistic configurations of the system along *path 1* and *path 2* are shown in Figure 4d–f, focusing only on the central cage—which the SF_6 molecule diffuses into and out of—and its closest cage neighbours, with all other cages omitted for clarity. For *path 1*, the passage of SF_6 into the void of the central cage is hindered by the cage to its left (Figure 4e), as the two cages pack in a vertex-to-window manner. For *path 2*,

the two cage molecules dominating the diffusion process stack along the channel direction in an arene-to-window manner; the diffusion pathway traverses the narrow gas in-between the central cage and the one under it (Figure 4f).

For both diffusion pathways, we report the potential of mean force, as well as the corresponding average constraint force from which the PMF was derived, for each point along the reaction coordinate (Figure 4b,c). To illustrate the key events during the diffusion process, we show MD snapshots extracted at the start and the end of the reaction coordinate, as well as at the points where the constraint force is a local extremum. On both pathways, the SF_6 molecule starts in a pore channel ($d = 0$ □, where d is the reaction coordinate), where the constraint forces it experiences average out to be close to zero over 500 ps with a sampling interval of 1 ps (Figure 4c). As SF_6 proceeds along the reaction coordinate toward the centre of the cage void, we first see a decrease in the PMF for both pathways (Figure 4b), meaning that it is energetically favourable for the SF_6 molecule in the pore channel to move toward the cage, owing to the attractive interactions between SF_6 and the channel wall. The SF_6 molecule is more strongly adsorbed onto the channel wall along *path 1* than *path 2*, indicated by the significantly deeper energy well in the PMF profile of the former. The reason for this marked difference is that *path 1* traverses a small 'pocket'—formed by the vertices of the central cage and three neighbouring cages (coloured blue, orange, pink and purple in Figure 5)—that serves as a strong adsorption site for SF_6 (Figure 5b). By contrast, no such 'pockets' on the channel wall are on path 2, though there is a weak, but still favourable, site for SF_6 (Figure 6b).
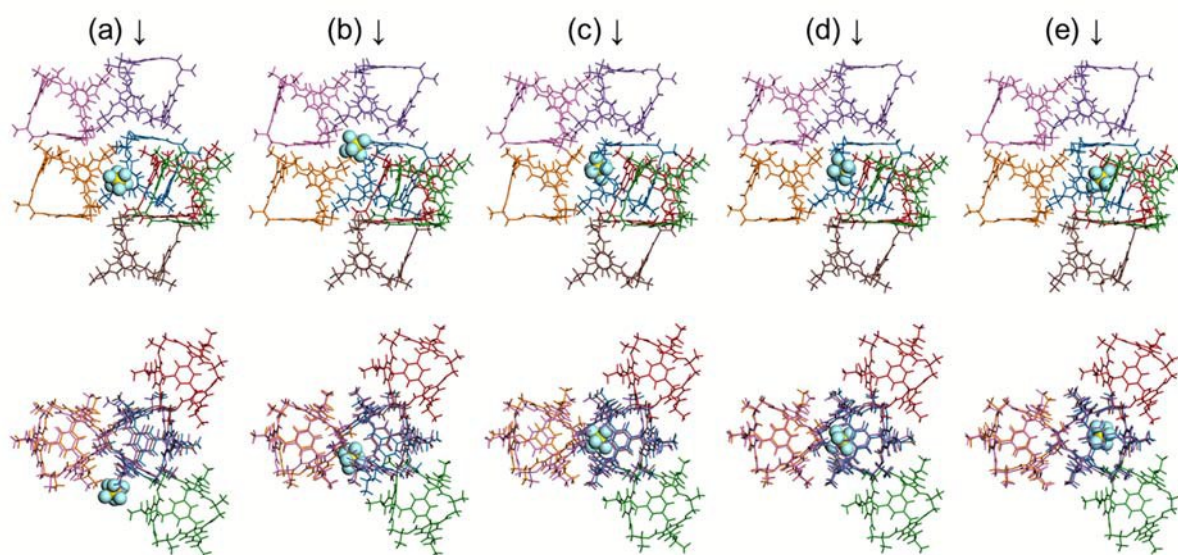

Figure 5. Cage molecules surrounding *path 1* in **α-CC2**, coloured individually: blue, the central cage into which SF_6 diffuses; orange, the cage that packs vertex-to-window with the central cage. Different points along the reaction coordinate (d) are displayed—d equals to 0.0, 1.8, 5.0, 5.8, and 9.4 □ in a–e, respectively—and viewed parallel to (top) and along (bottom) the pore channel direction.
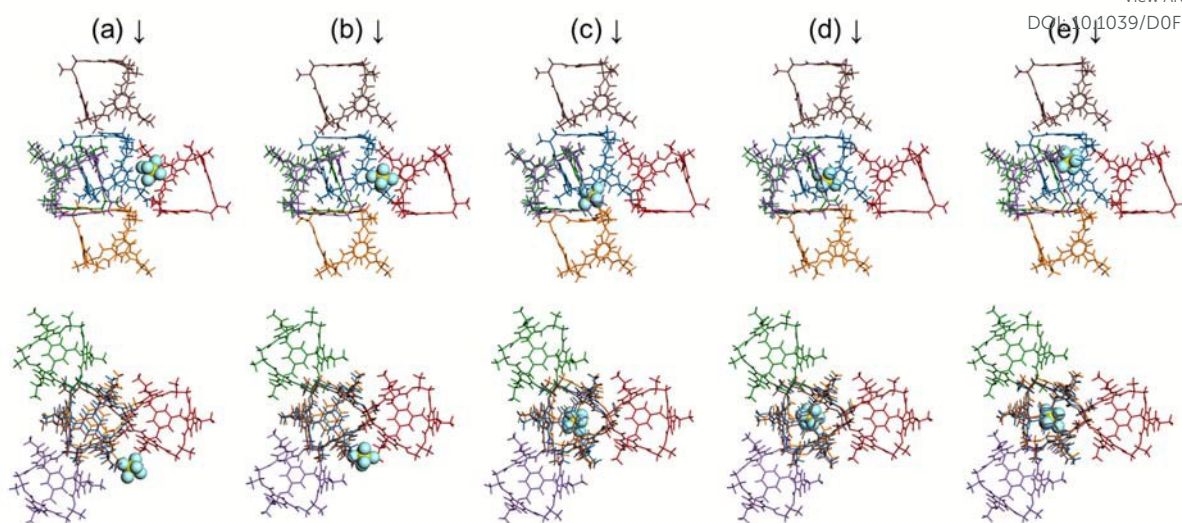
Figure 6. Cage molecules surrounding *path 2* in **α-CC2**, coloured individually: blue, the central cage into which SF_6 diffuses; orange, the cage that packs arene-to-window with the central cage. Different points along the reaction coordinate (*d*) are displayed—*d* equals to 0.0, 1.6, 2.8, 6.0, and 9.0 □ in a–e, respectively—and viewed parallel to (top) and along (bottom) the pore channel direction.

After the initial, adsorptive interactions between SF_6 and the channel wall, both diffusion pathways quickly start to go uphill in the potential of mean force (Figure 4b). The barriers to the SF_6 diffusion along *path 1* and *path 2* are calculated to be 40.8 and 40.9 kcal mol^{-1}, respectively. These barriers are very high compared to the barrier of 9.6 kcal mol^{-1} to the SF_6 diffusion through the window of **CC3**,[25] a closely related porous organic cage molecule to **CC2**. The much larger diffusion barriers in our cases are expected because here the PMF profiles are calculated for SF_6 diffusion through the solid-state structures of **CC2**, requiring the SF_6 molecule to force through the cage window blocked by the adjacent cage. By contrast, the much lower diffusion barrier of **CC3** was simulated using a single cage molecule in vacuum. Close inspection of the system configuration (Figure 5c) on *path 1* when the average constraint force is at its maximum (*d* = 5.0 □) shows that the barrier crossing event induces a local, albeit small, rearrangement of the neighbouring cages around the diffusion pathway. On *path 2*, the cage (coloured orange, Figure 6c top) that stacks arene-to-window with the central cage is deformed markedly to allow the passage of SF_6 into the void of the central cage. Clearly, both such local rearrangement of cages (*path 1*) and molecular deformation (*path 2*) come at an extra free-energy cost to the one arising from crossing the cage window. It is conceivable that having the pore channels filled with SF_6 may help it overcome the high energy barriers to diffusing into the cage voids. However, it should be noted that the diffusion barriers calculated here may have been artificially raised, at least, partly due to the finite simulation cells with periodic boundary conditions. In addition, the simulation cells were restrained to maintain the hexagonal crystal lattice—that is, the simulation cells did not change their shape during the NPT-MD simulations—to ensure stability of the system when the constraint force was applied.

This likely also contributed to the high diffusion barriers. Once past the point of inflection, the increase in the PMF, for both *path 1* and *path 2*, starts to tail off, as a result of the decreasing constraint force (Figure 4b,c). This is because the SF_6 molecule moves away from the constricted window aperture toward the cage void, where its dynamics are greatly improved (Figures 5d,e and 6d,e).

It is not surprising that the SF_6 diffusion from the pore channels to the cage voids entails crossing of a high free-energy barrier, since the cage voids of the static single crystal structure of **α-CC2** are isolated and inaccessible even to H_2. Dynamic porosity, arising from transient pore network formation between the cage voids and the pore channels, to H_2 was observed in previous MD simulations;[24] that is, MD can simulate opportunistic hopping of H_2 into the cage voids when transient channels are formed as a result of the thermal motions of the cages. For H_2, *path 1* is the route that H_2 takes to enter the cage void, as a transient channel is formed at the vertex-to-window packing motif between the two neighbouring cages. However, larger gas molecules, such as CO_2 and Xe, cannot take advantage of such transient channels, which are still too small to allow passage of large gases. For diffusion of large guest molecules in **α-CC2**, including SF_6, cooperative porosity is essential, where the diffusing guest influences the host structure: for example, resulting in a channel opening event that facilitates guest transport. To probe the cooperative character of SF_6 diffusion along *path 1* and *path 2*, we calculated the dynamic size distributions of the pore, window and maximum dimension of the $CC2$ cages on the MD trajectories of the same characteristic points on the PMF profiles as in Figures 5 and 6. We performed our calculations and analyses on individual cage molecules during the course of each trajectory to show how molecules behaved and evolved over time at the different points of the diffusion process. We focused on the central cage, into which SF_6 diffuses, and its five direct neighbours, in the case of *path 2* (Figure 8), and plus one extra nearby cage, part of the strong adsorption site for SF_6, in the case of *path 1* (Figure 7). The same cage molecules are illustrated in Figures 5 and 6 for *path 1* and *path 2*, respectively; the cages are coloured consistently between Figures 5 and 7, and between Figures 6 and 8. For comparison, we also sampled the equivalent size distributions for three reference cages on each of the same MD trajectories; these cages are away from the cages of interest to SF_6 diffusion in the simulation box.
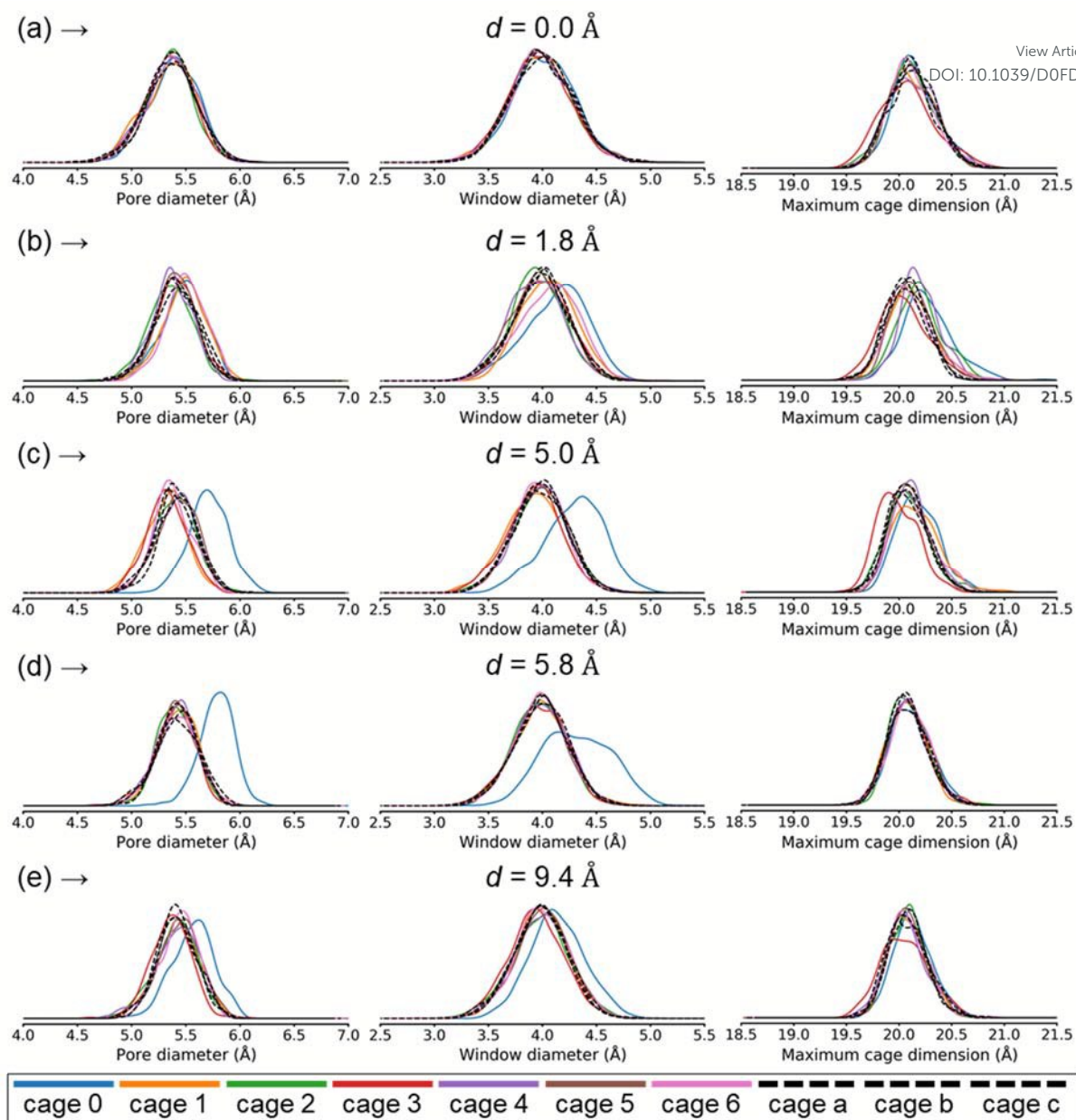
Figure 7. Dynamic size distributions of the pore diameter, window diameter, and maximum molecular dimension of the **CC2** cage molecules, sampled over 500 ps NPT-MD trajectories constrained to five characteristic points (a–e) on the reaction coordinate (*d*) for *path 1*. Cages 0–6 are around the SF_6 diffusion pathway, with cage 0 being the central cage into which SF_6 diffuses and cage 1 being the cage that packs vertex-to-window with cage 0. Cages a–c are reference cages far away from cages 0–6. Cages 0–6 are colour-coded the same as they are in Figure 5.
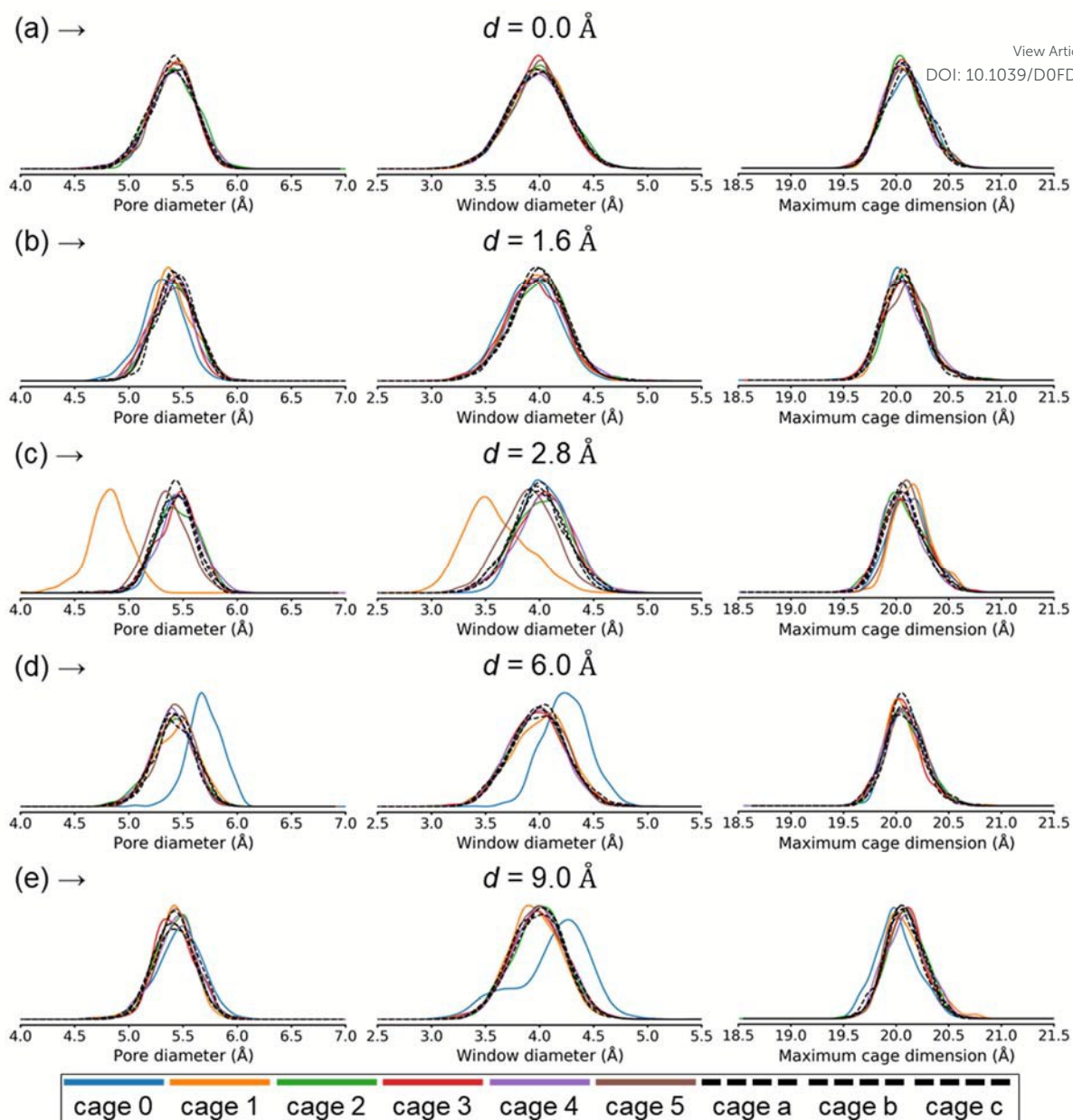
Figure 8. Dynamic size distributions of the pore diameter, window diameter, and maximum molecular dimension of the **CC2** cage molecules, sampled over 500 ps NPT-MD trajectories constrained to five characteristic points (a–e) on the reaction coordinate (*d*) for *path 2*. Cages 0–5 are around the SF_6 diffusion pathway, with cage 0 being the central cage into which SF_6 diffuses and cage 1 being the cage that packs arene-to-window with cage 0. Cages a–c are reference cages far away from cages 0–5. Cages 0–5 are colour-coded the same as they are in Figure 6.

At the start of *path 1* ($d = 0.0$ □), the SF_6 molecule is located in the pore channel, and the distributions of the pore, window and maximum molecular dimension for all of the cages sampled are almost the same (Figure 7a). There are no significant differences between the cages (0–6) involved in the diffusion pathway and the reference cages (a–c), in terms of their dynamic size distributions. This is also the case at the start of *path 2* (Figure 8a). When the SF_6 molecule binds to the strong adsorption 'pocket'—formed by the four cages coloured blue,

orange, pink and purple in Figure 5b—on *path 1* (d = 1.8 Å, Figure 7b), the surrounding cages show slightly enlarged pore diameters and more pronounced increases in their window diameters, compared to both the reference cages and the other two coloured cages. By contrast, when SF_6 adsorbs on the much weaker adsorption site on *path 2* (d = 1.6 Å, Figure 8b), all cages remain almost unperturbed except the central cage showing a small decrease in its pore diameter and window diameter.

At the maximum of the constraint force (*path 1*: d = 5.0 Å, Figure 7c; *path 2*: d = 2.8 Å, Figure 8c), when the SF_6 molecule pushes the hardest to go through the bottleneck on the pathway, the cooperative characters are distinctly different between *path 1* and *path 2*. For *path 1*, the central cage, into which SF_6 diffuses, is expanded, while the adjacent cages get compressed showing appreciable decreases in their pore diameters and window diameters. However, a different mechanism is at play in facilitating the passage of SF_6 into the central cage, at the equivalent point on *path 2*. All cages maintain very similar dynamic size distributions, including the central cage, except the cage (cage 1, Figure 8c) that stacks arene-to-window with the central cage, which is considerably squashed by SF_6, with the arene blocking the cage window of the central cage markedly pushed inwards (Figure 6c, top). As the SF_6 molecule continues to diffuse into the void of the central cage, which stays expanded, all other cages relax back to their equilibrium geometries and dynamics, barely distinguishable from the reference cages (Figure 7d,e and Figure 8d,e).

Finally, we performed analyses of displacive movements of the above-discussed cage molecules surrounding *path 1* and *path 2* (Figure 9), using the same MD snapshots as for the calculations of dynamic size distributions of the cages (Figures 7 and 8). We followed the centre of mass (COM) of each cage molecule of interest over the MD trajectories at the characteristic points of the reaction coordinate as discussed above. The root-mean-squared displacement (RMSD) of each COM over the MD trajectories, with reference to the last configuration of the MD trajectory at the start (d = 0.0 Å) of the diffusion path (that is, SF_6 in the pore channel), is used as the measure of the spatial extent of flexibility of these cage molecules. Overall, no dramatic movements of the whole cage are observed for all the cages (Figure 9), which indicates a robustness of the crystal packing of **α-CC2**, corroborating our *in-situ* diffraction results. The largest COM movements among all the systems sampled are observed for cage 1—which packs arene-to-window with the central cage (cage 0)—when at the constraint-force maximum on *path 2*, moving off its equilibrium position by 1.5–2.0 Å (Figure 9b, d = 2.8 Å). However, this seemingly large displacement is mostly accounted for by its significantly reduced pore diameter (Figure 6c, top; Figure 8c) as a result of the SF_6 molecule forcing its way through the narrow opening of the arene-to-window packing motif. These RMSD analyses indicate that the diffusion of SF_6 into the cage void does not cause the cage molecules on its pathway to deviate dramatically from their equilibrium positions in the crystal lattice, in line with our observations in the *in-situ* diffraction experiments. Instead, small cooperative movements of the cage molecules, combined with their molecular flexibility, can facilitate the diffusion of SF_6 into the cage voids that are

apparently isolated in a static view of the crystal structure. Overall, our simulations seem to suggest that *path 1* may be the more probable diffusion pathway, compared to *path 2*, for SF_6 to enter the cage voids in **α-CC2**. The reason is threefold: (1) there is a strong adsorption site for SF_6; (2) the barrier-crossing process necessitates only cooperativity of the cages in the immediate vicinity; (3) no significant deformation to cage molecules is required except for the cage adsorbing SF_6 in its void.
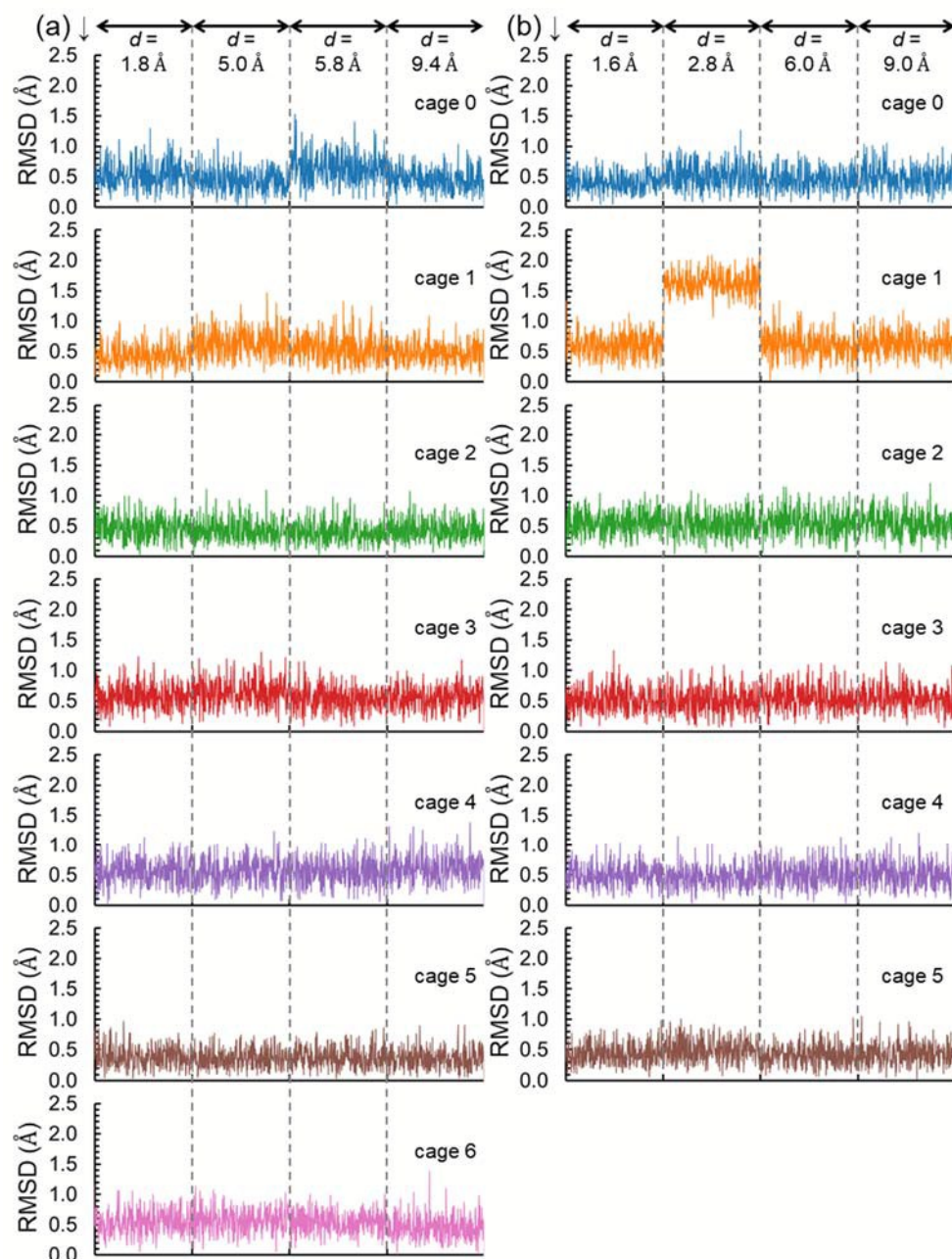
Figure 9. Root-mean-squared displacement (RMSD) of the centre of mass of individual cage molecules during the MD trajectories (last 500 ps) for the different points on *path 1* (a) and *path 2* (b). Each RMSD is referenced to the respective, final configuration of the system at the start of the diffusion pathway, *i.e.*, SF_6 in the channel and $d = 0.0$ □.

Conclusions

In summary, we have combined *in situ* diffraction experiments and molecular dynamics simulations to understand the adsorption of SF_6 in the porous cage crystal, **α-CC2**. Our PXRD data show unambiguously that SF_6 is present in both the extrinsic channel (71(2)% mean occupancy of two channel sites) and also in the intrinsic cage cavity (52(2)% of the cage sites occupied). The packing of **CC2** molecules in SF_6-loaded structures is largely undisrupted compared to the empty **α-CC2** structure, despite the cage voids being apparently occluded from the pore channels according to a 'static' pore analysis of these SF_6-loaded structures. Molecular dynamics simulations, coupled with a 'dynamic' analysis of the molecular pores of **CC2** cages, show that SF_6 can diffuse into the cage voids in **α-CC2** by overcoming a free energy barrier imposed by the constricted cage windows. Cooperative movements of a small number of cages in close proximity can facilitate the passage of SF_6 into the cage void, without perturbing the crystal packing beyond the small local environment around the diffusion pathway. This work highlights the importance of the ubiquitous cooperative phenomena in soft porous molecular crystals, and both the design challenges and opportunities that this affords. Specifically, cooperative diffusion can lend such soft materials unexpected and often arresting properties that are governed by both the structure and the inherent dynamics of the material. We note that such properties are still extremely challenging to design in an *a priori* sense, but molecular calculations are useful for rationalizing and understanding these complex cooperative phenomena.

Conflicts of interest

There are no conflicts to declare.

Acknowledgements

Notes and references

1   E. M. Miner and M. Dincă, *Philos. Trans. R. Soc. A Math. Phys. Eng. Sci.*, 2019, 377.

2   A. Dhakshinamoorthy, Z. Li and H. Garcia, *Chem. Soc. Rev.*, 2018, 47, 8134–8172.

3   M. H. Teplensky, M. Fantham, C. Poudel, C. Hockings, M. Lu, A. Guna, M. Aragones-Anglada, P. Z. Moghadam, P. Li, O. K. Farha, S. Bernaldo de Quirós Fernández, F. M. Richards, D. I. Jodrell, G. Kaminski Schierle, C. F. Kaminski and D. Fairen-Jimenez, *Chem*, 2019, **5**, 2926–2941.

4   S. Horike, S. Shimomura and S. Kitagawa, *Nat. Chem.*, 2009, 1, 695–704.

5   G. R. Krishna, R. Devarapalli, G. Lal and C. M. Reddy, *J. Am. Chem. Soc.*, 2016, **138**, 13561–13567.

6   L. Li, P. Commins, M. B. Al-Handawi, D. P. Karothu, J. M. Halabi, S. Schramm, J. Weston, R. Rezgui and P. Naumov, *Chem. Sci.*, 2019, **10**, 7327–7332.

7   L. Sun, B. Liao, D. Sheberla, D. Kraemer, J. Zhou, E. A. Stach, D. Zakharov, V. Stavila, A. A. Talin, Y. Ge, M. D. Allendorf, G. Chen, F. Léonard and M. Dincă, *Joule*, 2017, **1**, 168–177.

8   A. I. Kitaigorodskii, *Acta Crystallogr.*, 1965, **18**, 585–590.

9   W. Yang, A. Greenaway, X. Lin, R. Matsuda, A. J. Blake, C. Wilson, W. Lewis, P. Hubberstey, S. Kitagawa, N. R. Champness and M. Schröder, *J. Am. Chem. Soc.*, 2010, **132**, 14457–14469.

10   Y. He, S. Xiang and B. Chen, *J. Am. Chem. Soc.*, 2011, **133**, 14570–14573.

11   H. Wang, B. Li, H. Wu, T. L. Hu, Z. Yao, W. Zhou, S. Xiang and B. Chen, *J. Am. Chem. Soc.*, 2015, **137**, 9963–9970.

12   R. B. Lin, Y. He, P. Li, H. Wang, W. Zhou and B. Chen, *Chem. Soc. Rev.*, 2019, 48, 1362–1389.

13   Q. Huang, W. Li, Z. Mao, L. Qu, Y. Li, H. Zhang, T. Yu, Z. Yang, J. Zhao, Y. Zhang, M. P. Aldred and Z. Chi, *Nat. Commun.*, , DOI:10.1038/s41467-019-10575-5.

14   T. Tozawa, J. T. A. Jones, S. I. Swamy, S. Jiang, D. J. Adams, S. Shakespeare, R. Clowes, D. Bradshaw, T. Hasell, S. Y. Chong, C. Tang, S. Thompson, J. Parker, A. Trewin, J. Bacsa, A. M. Z. Slawin, A. Steiner and A. I. Cooper, *Nat. Mater.*, 2009, **8**, 973–978.

15   M. Liu, L. Zhang, M. A. Little, V. Kapil, M. Ceriotti, S. Yang, L. Ding, D. L. Holden, R. Balderas-Xicohténcatl, D. He, R. Clowes, S. Y. Chong, G. Schütz, L. Chen, M. Hirscher and A. I. Cooper, *Science*, 2019, **366**, 613–620.

16   G. Zhang, O. Presly, F. White, I. M. Oppel and M. Mastalerz, *Angew. Chemie Int. Ed.*, 2014, **53**, 1516–1520.

17   A. Avellaneda, P. Valente, A. Burgun, J. D. Evans, A. W. Markwell-Heys, D. Rankine, D. J. Nielsen, M. R. Hill, C. J. Sumby and C. J. Doonan, *Angew. Chemie Int. Ed.*, 2013, **52**, 3746–3749.

18   M. Kato, H. Ito, M. Hasegawa and K. Ishii, *Chem.Eur. J.*, 2019, **25**, 5105–5112.

19   V. López-Mejías, J. W. Kampf and A. J. Matzger, *J. Am. Chem. Soc.*, 2012, **134**, 9872–9875.

20   J. P. Brog, C. L. Chanez, A. Crochet and K. M. Fromm, *RSC Adv.*, 2013, 3, 16905–16931.

21   Y. Sagara and T. Kato, *Nat. Chem.*, 2009, **1**, 605–610.

22   Y. Zhou, F. Guo, C. E. Hughes, D. L. Browne, T. R. Peskett and K. D. M. Harris, *Cryst. Growth Des.*, 2015, **15**, 2901–2907.

23   H. Sakamoto, T. Fujimori, X. Li, K. Kaneko, K. Kan, N. Ozaki, Y. Hijikata, S. Irle and K. Itami, *Chem. Sci.*, 2016, **7**, 4204–4210.

24   D. Holden, S. Y. Chong, L. Chen, K. E. Jelfs, T. Hasell and A. I. Cooper, *Chem. Sci.*,

2016, **7**, 4875–4879.

25   T. Hasell, M. Miklitz, A. Stephenson, M. A. Little, S. Y. Chong, R. Clowes, L. Chen, D. Holden, G. A. Tribello, K. E. Jelfs and A. I. Cooper, *J. Am. Chem. Soc.*, 2016, **138**, 1653–1659.

26   L. J. Barbour, *Chem. Commun.*, 2006, 1163–1168.

27   J. L. Atwood, L. J. Barbour, A. Jerga and B. L. Schottel, *Science*, 2002, **298**, 1000–1002.

28   S. Y. Chong and A. I. Cooper, in *Comprehensive Supramolecular Chemistry II*, Elsevier Inc., 2017, vol. 6, pp. 139–197.

29   Z. Wang, N. Sikdar, S.-Q. Wang, X. Li, M. Yu, X.-H. Bu, Z. Chang, X. Zou, Y. Chen, P. Cheng, K. Yu, M. J. Zaworotko and Z. Zhang, *J. Am. Chem. Soc.*, 2019, **141**, 9408–9414.

30   F. Beuerle and B. Gole, *Angew. Chemie - Int. Ed.*, 2018, 57, 4850–4878.

31   M. A. Little, S. Y. Chong, M. Schmidtmann, T. Hasell and A. I. Cooper, *Chem. Commun.*, 2014, **50**, 9465–9468.

32   L. Chen, P. S. Reiss, S. Y. Chong, D. Holden, K. E. Jelfs, T. Hasell, M. A. Little, A. Kewley, M. E. Briggs, A. Stephenson, K. M. Thomas, J. A. Armstrong, J. Bell, J. Busto, R. Noel, J. Liu, D. M. Strachan, P. K. Thallapally and A. I. Cooper, *Nat. Mater.*, 2014, **13**, 954–960.

33   T. Mitra, K. E. Jelfs, M. Schmidtmann, A. Ahmed, S. Y. Chong, D. J. Adams and A. I. Cooper, *Nat. Chem.*, 2013, **5**, 276–281.

34   J. S. Camp and D. S. Sholl, *J. Phys. Chem. C*, 2016, **120**, 1110–1120.

35   J. E. Parker, J. Potter, S. P. Thompson, A. R. Lennie and C. C. Tang, in *Materials Science Forum*, 2012, vol. 706–709, pp. 1707–1712.

36   A. A. Coelho, *J. Appl. Crystallogr.*, 2018, **51**, 210–218.

37   I. T. Todorov, W. Smith, K. Trachenko and M. T. Dove, *J. Mater. Chem.*, 2006, **16**, 1911–1918.

38   C. W. Yong, *J. Chem. Inf. Model.*, 2016, **56**, 1405–1409.

39   J. L. Banks, H. S. Beard, Y. Cao, A. E. Cho, W. Damm, R. Farid, A. K. Felts, T. A. Halgren, D. T. Mainz, J. R. Maple, R. Murphy, D. M. Philipp, M. P. Repasky, L. Y. Zhang, B. J. Berne, R. A. Friesner, E. Gallicchio and R. M. Levy, *J. Comput. Chem.*, 2005, 26, 1752–1780.

40   A. Olivet and L. F. Vega, *J. Chem. Phys.*, , DOI:10.1063/1.2714953.

41   M. Miklitz and K. E. Jelfs, *J. Chem. Inf. Model.*, 2018, **58**, 2387–2391.

42   T. Hasell, S. Y. Chong, K. E. Jelfs, D. J. Adams and A. I. Cooper, *J. Am. Chem. Soc.*, 2012, **134**, 588–598.

43   S. Kawahara, S. Tsuzuki and T. Uchimaru, *J. Phys. Chem. A*, 2004, **108**, 6744–6749.

44   P. Li, J. M. Maier, E. C. Vik, C. J. Yehl, B. E. Dial, A. E. Rickher, M. D. Smith, P. J. Pellechia and K. D. Shimizu, *Angew. Chemie Int. Ed.*, 2017, **56**, 7209–7212.